Renewable Energy 131 (2019) 1060–1072

Contents lists available at ScienceDirect

Renewable Energy

journal homepage: www.elsevier.com/locate/renene

Analysis and optimization of a Dual Mass-Spring-Damper (DMSD) wave-energy convertor with variable resonance capability

Zhongfei Chen [a], Liang Zhang [a, *], Ronald W. Yeung [b, *]

[a] College of Shipbuilding Engineering, Harbin Engineering University, Harbin, 150001, China
[b] Director, The Berkeley Marine Mechanics Laboratory, University of California at Berkeley, Berkeley, CA 94720, USA

ARTICLE INFO

Article history:
Received 14 June 2017
Received in revised form
7 June 2018
Accepted 2 July 2018
Available online 11 July 2018

Keywords:
Wave-energy conversion
Dual-mass-spring-damper
Variable resonance-frequency capability
Time-domain solution
Motion limitations
Irregular-wave response

ABSTRACT

To adapt to an ocean environment of changing wave period, a novel point-absorber concept is proposed: a fully-enclosed Dual Mass-Spring-Damper (DMSD) floater system that has an internal mass and spring so that its resonance frequency can be varied by changing the movable internal mass and spring. In a waterproof floater, this one-degree-of-freedom heaving energy converter can float or be submerged to evade excessive storm load. Optimization of the internal mass, spring and damping system in the frequency domain is first developed to demonstrate that favorable capture width is achievable for a range of incident-wave frequency. Next, power and motion response of this system in an ISSC wave spectrum are studied in time domain. With constant damping for power-takeoff, the DMSD system is found to have noticeably lower capture width in irregular waves than that in regular waves at a frequency that is the same as the peak wave frequency of the spectrum. Since excessive relative motion can occur in irregular-wave excitation, end-stops, modeled by a stiff spring and strong damper, are applied in the time-domain simulation. When properly designed, degradation of only 1–2% in the capture width in the irregular-wave environment is found when end-stops are applied.

1. Introduction

Wave energy is probably the most promising type of renewable energy because of its high energy density and predictability [1]. The worldwide potential of wave energy is estimated about 2 Tera-Watts, which is almost equal to the world energy consumption [2]. In an open sea, wave frequency changes continuously in time scale of seconds, minutes, or hours. Traditional point absorber, which typically has one resonance frequency with a narrow bandwidth, cannot work as effectively at different wave periods. Compared to wind energy, which can start from small size to large ones gradually, working equally well regardless of the size, WEC has to be built to match the wave frequency for an effective energy capture. At 10s wave period, the required characteristic dimension would be 20 m [3], thus calling for an expensive capital outlay, a possible explanation of the slow development of the wave-energy industry. This paper represents a novel WEC concept called Dual Mass-Spring-Damper (DMSD) system. With two sets of mass and spring, the response of the system can be controlled so that the resonance frequency of the DMSD can better match the changing wave environment. The first set of mass-spring is the total mass of the floater with hydrostatic restoring associated with the waterplane area while another mass-spring system is inside the floater (Fig. 2.1 (a)). This contrasts the traditional arrangement shown, for example, in Ref. [4]. Because the resonance frequency of DMSD is controllable, this variable resonance capability provides the idea to examine a relatively small device in laboratory environment. Finally, as proposed here, all moving parts (internal mass, spring and linear generator etc.) are contained in a waterproof floater, so, the floater can be operating on the surface or submerged to avoid excessive loads due to storm. To be complete, there are also now control strategies to handle the typical traditional design in random waves to broaden the capturing bandwidth, see e.g., Tom & Yeung [5].

WEC with two mass system was studied by Parks [6], French [7], Chaplin [8], Wang et al. [9] etc. In Parks' work, he used fixed spring stiffness though he varied the damping, whereas French also varied the spring. The device “Frog” described in Chaplin's work was a WEC with a transverse mass block, working in pitch mode. Later, Korde [10,11] compared the performance between a WEC with

* Corresponding authors.
E-mail addresses: zhangliang@hrbeu.edu.cn (L. Zhang), rwyeung@berkeley.edu (R.W. Yeung).

https://doi.org/10.1016/j.renene.2018.07.006
0960-1481/© 2018 Published by Elsevier Ltd.

Nomenclature

Φ	total velocity potential that depends on (x,y,z,t)
ϕ_0 & ϕ_7	incident-wave and diffracted-wave spatial potential
ϕ_i	body radiation spatial potential of i-th mode
A_w	wave amplitude of regular wave
a_i	body motion amplitude of i-th mode
$\overline{\mu}_{ij}$ & μ_{ij}	non-dimensional & dimensional added mass
$\overline{\lambda}_{ij}$ & λ_{ij}	non-dimensional & dimensional radiation damping alone
$\overline{\lambda}_T$ & λ_T	non-dimensional & dimensional total damping of heave mode
f_{vis}	viscous effect factor for damping of heave mode
$\overline{f}_{ej}$ & f_{ej}	non-dimensional & dimensional wave-excitation force of direction j
$\overline{X}_j$ & X_j	non-dimensional & dimensional wave excitation force per unit wave amplitude
a, d	radius and draft of the cylindrical floater
h	water depth
$\overline{\omega}$ & ω	non-dimensional & dimensional wave angular frequency
ζ	incident-wave elevation
x_3	motion of the floater in global coordinate system
x_{3m}	motion of the internal mass in the global coordinate system
x_r	relative motion between the internal mass and the floater
M	total mass of the entire DMSD system (mass of the floater and mass of the internal mass)
$\overline{m}$ & m	non-dimensional mass normalized by M & dimensional mass of the internal mass
C_3	hydrostatic restoring force coefficient in heave
$\overline{B}_g$ & B_g	non-dimensional & dimensional damping coefficient of the PTO system
$\overline{s}$ & k_m	non-dimensional & dimensional spring coefficient between the mass block and the floater
$\overline{\omega}$ & ω_3	non-dimensional & dimensional resonant frequency of the floater
ω_m	resonant frequency of the floater of the internal system
$\overline{\Omega}_{1,2}$ & $\Omega_{1,2}$	non-dimensional & dimensional (lower and higher) resonant frequency of the DMSD system
M'	effective mass (of floater) $= M + \mu_{33} - m$
P_M	power extraction by the PTO
$\overline{P}_W$	time-averaged wave power in unit width
$\overline{C}_w$	capture width ratio, normalized by WEC diameter
$K_{33}(t)$	retardation function of heave mode
T_p	peak period of wave spectrum
H_s & A_s	significant wave height and significant wave amplitude
$\overline{\omega}_p$	non-dimensional wave peak frequency
$\overline{B}_e$ & B_e	non-dimensional & dimensional damping coefficient of the End-stop
$\overline{k}_e$ & k_e	non-dimensional & dimensional spring coefficient of the End-stop
$\overline{L}_e$ & L_e	non-dimensional & dimensional length of the End-stop

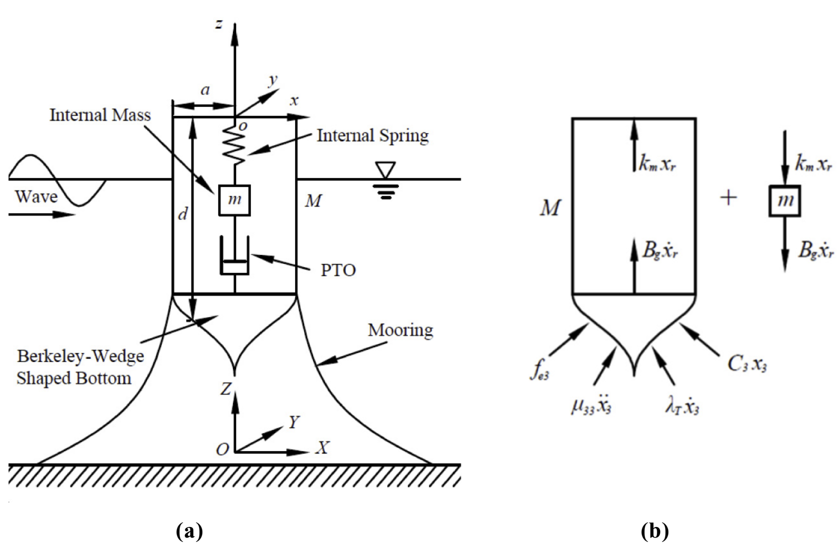

Fig. 2.1. Schematic for (a) Dual-MSD concept with fixed-on earth coordinates (OXYZ) and moving coordinates (oxyz) and (b) forces on the moving floater and the internal mass.

mass plate above the converter and WEC with plate submerged. The WEC with mass plate onboard as a motion compensator was examined. Wang et al. [9] studied a dual co-axial cylinder WEC, working in heave mode using linear generator as the power take-off (PTO).

This paper studies the resonance frequency of the Dual-MSD coupled system and the influence of internal properties on the motion and power response in the frequency domain. Optimization of capture width is first conducted by using frequency domain analysis. Since the relative motion is limited by the vertical extent of the encasing floater, so the capture width is not only a function of wave frequency but also a function of wave amplitude, a nonlinear feature of this problem. Time-domain analysis given here in irregular wave for the internal mass system working in heave mode is the first of its kind. The Impulse Response Function (IRF) method [12] is used with the ISSC [13] spectrum to simulate the behavior in irregular waves and serves also as a cross-check of the frequency-domain results. In irregular seas, excessive relative motion occurs sometimes because the irregularity of the waves, thus an "end-stop" is introduced, which is modeled by stiff spring, damper, traverse length. With proper design, the end-stop not only can effectively restrain the relative motion in irregular wave, but also cause little energy loss (around 1–2%).

2. Frequency-domain analysis

2.1. Hydrodynamics of the floater shell

As shown in Fig. 2.1 (a), the floater is a heaving axisymmetrical cylinder with a Berkeley-Wedge shaped bottom [14]. It is insensitive to the incident wave angle. The Berkeley Wedge is a patented two-dimensional shape, meant to decrease the viscous effect and to enhance larger motion and better energy capture. To define the hydrodynamic forces, we assume that the fluid is inviscid, incompressible and flow irrotational. The total velocity potential $\Phi(x,y,z,t)$ is given by Eq. (2.1).

$$\Phi(x,y,z,t) = \Re\left\{A_w[\varphi_0(x,y,z) + \varphi_7(x,y,z)]e^{-i\omega t}\right\} + \Re\left\{\varphi_i(x,y,z)A_i(-i\omega)e^{-i\omega t}\right\} \tag{2.1}$$

where ϕ_0 is the incident wave spatial potential. ϕ_7 is the diffraction wave spatial potential. ϕ_i is the radiation spatial potential body for direction i. Because we only consider heave motion in this design, so i=3. The hydrodynamic added mass μ_{ij} and radiation damping λ_{ij} act in j-direction due to the motion in the i-direction:

$$\mu_{ij} + i\frac{\lambda_{ij}}{\omega} = \rho \int_{S_B} \varphi_i n_j dS \tag{2.2}$$

The wave-exciting force f_{ej} is given by incident wave and diffraction wave (Eq. (2.4))

$$f_{ej} = \Re\left\{A_w X_j e^{-i\omega t}\right\} \tag{2.3}$$

$$X_j = |X_j|e^{i\delta_j} = i\rho\omega \int_{S_B} [\varphi_0 + \varphi_7] n_j dS \tag{2.4}$$

$$\zeta(x,t) = \Re\left\{A_w e^{i(k_0 x - \omega t)}\right\} \tag{2.5}$$

where ζ is the incident-wave elevation at x, time t. $|X_j|$ is the wave-exciting force amplitude per unit wave amplitude and δ_j is the phase angle, relative to incident wave elevation at x = 0.

These hydrodynamic quantities were solved using a semi-analytical theory developed by Yeung [15]. This in-house code is on a UC-Berkeley server for public access. For the convenience of the planned experimental work, the overall geometry of the floater is taken *as: 2a/h*=0.271 and $d/h = 0.288$, where a is the radius, d is the draft of the cylinder, and h is the water depth. For the wave tank at UC Berkeley Richmond Field Station Physical-Model Testing Facility, the water depth is $h = 1.5$ m [16]. In Fig. 2.1(a) the draft d is an equivalent draft, which so that submerged mass of The Berkeley Wedge will have the same resonance frequency of the Dual-MSD floater with the flat-bottom cylinder.

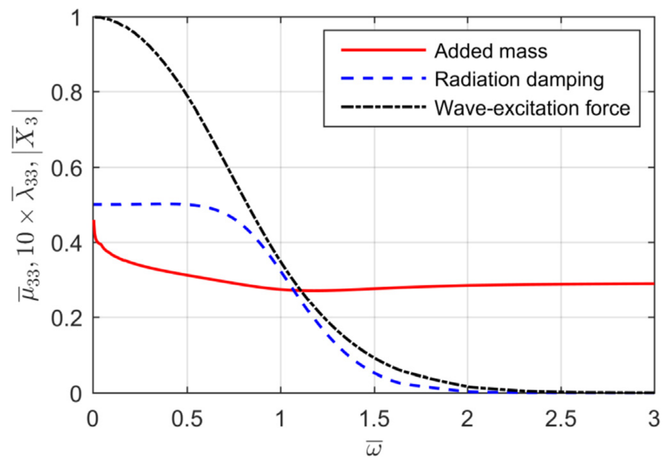

Fig. 2.2. Non-dimensional hydrodynamic properties (using [15]) of a vertical cylinder, $2a/h = 0.271$ and $d/h = 0.288$.

Fig. 2.2 shows the hydrodynamic properties (added mass, radiation damping and wave-excitation force) for the given geometry. The non-dimensionaiizations are $\overline{\mu}_{33} = \mu_{33}/\pi\rho a^2 d$, $\overline{\lambda}_{33} = \lambda_{33}/\omega\pi\rho a^2 d$, $\overline{X}_3 = X_3/\pi\rho a^2$ and $\overline{\omega} = \omega\sqrt{a/g}$, and $C_3 = \rho g A_{wp}$, where A_{wp} is the waterplane area of the floater. To model realistic viscous effects on the floater, we recall some experimental data from Son [16], in which he took advantage of the Berkeley-Wedge shape and applied it to an axisymmetric geometry. It was found that the total damping (radiation damping plus equivalent linear viscous damping) became roughly one third of that of a flat bottom while the heave added mass was not much changed. Thus, we can use a viscosity-modified hydrodynamic damping coefficients of a flat-bottom cylinder as follows:

$$\lambda_T = (1 + f_{vis})\lambda_{33} \tag{2.6}$$

where f_{vis} is the viscous coefficient for damping and is body-shape dependent. For the Berkeley-Wedge shaped bottom, $f_{vis} \approx 1.753$.[1]

2.2. Equations of motion of the coupled system

Under the linear-wave and small-motion assumption, the heave motion is decoupled with motions of other freedoms (see Cochet [17]). In Fig. 2.1(a), *OXYZ* is the earth-fixed (global) coordinate system fixed on the sea bed and *oxyz* is the moving coordinate fixed on the floater. x_3 and x_{3m} represent the absolute vertical position of the floater and the mass block, respectively, relative to the global coordinate system *OXYZ*, thus $x_r \equiv x_{3m} - x_3$ defines the position of the internal mass block relative to the floater position.

From Fig. 2.1(b), we can develop the force balance of each of the mass system [11]:

$$(M - m)\ddot{x}_3 = f_{e3} - \mu_{33}\ddot{x}_3 - \lambda_T\dot{x}_3 - C_3 x_3 + B_g\dot{x}_r + k_m x_r \tag{2.7}$$

$$m\ddot{x}_{3m} = -B_g\dot{x}_r - k_m x_r \tag{2.8}$$

with B_g being the PTO damper coefficient. Here M is the mass of the entire coupled system (including both floater and the internal mass block), m represents the mass of the mass block, and k_m represents

[1] For the two-dimensional Berkeley Wedge [14], $f_{vis} \approx 0, f_{vis}$ can be measured using a transient free-decay heaving test. For a three-dimensional (axisymmetric) wedge $f_{vis} \approx 1.753$ [16], whereas a similarly measured value of a flat, truncated-bottom cylinder of the same proportions was $f_{vis} \approx 7.448$.

the spring between the mass block and the floater. $f_{e3} = \Re\{A_w X_3 e^{-i\omega t}\}$ is the wave excitation force given by Eq. (2.3). According to Bachynski et al. [4], the mooring system only introduces a low frequency resonance frequency and does not change the wave-frequency response of WEC, thus does not need to be considered. In a real system, mechanical friction may exist, which can be considered easily by modifying the term B_g in Eqs. (2.7) and (2.8). However, it is neglected in the present paper. In matrix form, it is convenient to write this 2-DOF system as:

$$\begin{bmatrix} M-m+\mu_{33} & 0 \\ 0 & m \end{bmatrix}\begin{Bmatrix} \ddot{x}_3 \\ \ddot{x}_{3m} \end{Bmatrix} + \begin{bmatrix} \lambda_T + B_g & -B_g \\ -B_g & B_g \end{bmatrix}\begin{Bmatrix} \dot{x}_3 \\ \dot{x}_{3m} \end{Bmatrix} + \begin{bmatrix} C_3 + k_m & -k_m \\ -k_m & k_m \end{bmatrix}\begin{Bmatrix} x_3 \\ x_{3m} \end{Bmatrix} = \begin{Bmatrix} f_{e3} \\ 0 \end{Bmatrix} \tag{2.9}$$

2.3. Coupled resonance frequencies of the Dual-MSD system

Similar in character to [11], this Dual-MSD has two un-damped resonance frequencies $\Omega_{1,2}$, the expressions for these are shown in Eqs. (2.11) with the damping neglected. Of interest, we observe that Ω_1 is lower than the resonance frequency of the floater itself ω_3, and that of the internal mass-spring ω_m without consideration of coupling, while the other frequency Ω_2 is higher.

$$\omega_3 = \sqrt{C_3/(M+\mu_{33}(\omega_3))}, \quad \omega_m = \sqrt{k_m/m} \tag{2.10}$$

$$\Omega_{1,2}^2 = \frac{1}{2}\frac{[1+\overline{\mu}_{33}(\overline{\omega}_3)](\omega_3^2+\omega_m^2)}{1+\overline{\mu}_{33}\left(\overline{\Omega}_{1,2}\right)-\overline{m}} \mp \frac{1}{2}\sqrt{\left(\frac{[1+\overline{\mu}_{33}(\overline{\omega}_3)](\omega_3^2+\omega_m^2)}{1+\overline{\mu}_{33}\left(\overline{\Omega}_{1,2}\right)-\overline{m}}\right)^2 - \frac{4\omega_3^2\omega_m^2[1+\overline{\mu}_{33}(\overline{\omega}_3)]}{1+\overline{\mu}_{33}\left(\overline{\Omega}_{1,2}\right)-\overline{m}}} \tag{2.11}$$

with $\Omega_1 < (\omega_3 \text{ and } \omega_m) < \Omega_2$.

In the above, three non-dimensional mass-ratios surface: $\overline{\mu}_{33}(\overline{\omega}_3) = \mu_{33}(\omega_3)/M$, and $\overline{\mu}_{33}(\overline{\Omega}_{1,2}) = \mu_{33}(\overline{\Omega}_{1,2})/M$[2] Here, $\overline{m} = m/M$ and $\overline{s} = k_m/C_3$ can be considered as parameters of the coupled system. For convenience, we rewrite Eq. (2.11) in non-dimensional with respect to $\overline{\omega}_3$ as

$$\overline{\Omega}_{1,2}^2 = \frac{1}{2}\frac{1+\overline{\mu}_{33}(\overline{\omega}_3)}{1+\overline{\mu}_{33}\left(\overline{\Omega}_{1,2}\right)-\overline{m}}\left[1+(1+\overline{\mu}_{33}(\overline{\omega}_3))\frac{\overline{s}}{\overline{m}}\right] \mp \frac{1}{2}\sqrt{\left(\frac{1+\overline{\mu}_{33}(\overline{\omega}_3)}{1+\overline{\mu}_{33}\left(\overline{\Omega}_{1,2}\right)-\overline{m}}\left[1+(1+\overline{\mu}_{33}(\overline{\omega}_3))\frac{\overline{s}}{\overline{m}}\right]\right)^2 - \frac{\overline{s}}{\overline{m}}\frac{4(1+\overline{\mu}_{33}(\overline{\omega}_3))}{1+\overline{\mu}_{33}\left(\overline{\Omega}_{1,2}\right)-\overline{m}}} \tag{2.12}$$

where $\overline{\Omega}_{1,2} = \Omega_{1,2}\sqrt{a/g}$ are the non-dimensional resonance frequencies of the fully coupled system, which need iterative solution using the added mass function, with the understanding that $\overline{\mu}_{33}(\overline{\omega}_3)$ is taken as constant once (2.10) has been iteratively solved.

The solution of Eq. (2.11) was obtained numerically by iteration using the known added-mass function $\overline{\mu}_{33}(\overline{\omega})$ from numerical data of Fig. 2.2. Fig. 2.3 displays $\overline{\Omega}_{1,2}$ as a function of $\overline{s}$ and $\overline{m}$. For certain given resonance frequency of $\overline{\Omega}_1$, more than one combination of $\overline{m}$ and $\overline{s}$ were possible. In addition, for a given or specified $\overline{\Omega}_1$, one may consider $\overline{s} = Q(\overline{m})$. Thus, a specific combination of $\overline{m}$ and $\overline{s}$ would yield a lower resonance-frequency value of such a Dual-MSD system. Finally, when $\overline{m} \to 0$ it implies that the DMSD system degenerates to a Single-MSD, $\overline{\Omega}_1 \to \overline{\omega}_3$, that is, the lower resonance frequency approaches that of a single-mass system, while the higher resonance frequency $\overline{\Omega}_2 \to +\infty$ since $\omega_m^2 = k_m/m \to +\infty$ in Eq. (2.11).

It is of more practical importance to work with the lower resonance frequency $\overline{\Omega}_1$. First, there is more ocean energy in lower frequency waves. Second, per Fig. 2.3, achieving a specific $\overline{\Omega}_1$is easier than that for $\overline{\Omega}_2$ because the former requires distinct values of $\overline{m}$ and $\overline{s}$ values to achieve it.

2.4. Motion and power response in regular waves

For notational simplicity, we define an effective mass $M' = M - m + \mu_{33}$ for the floater shell alone. The equation of motion of the Dual-MSD Eq. (2.9) now becomes:

$$\begin{bmatrix} M' & 0 \\ 0 & m \end{bmatrix}\begin{Bmatrix} \ddot{x}_3 \\ \ddot{x}_{3m} \end{Bmatrix} + \begin{bmatrix} \lambda_T + B_g & -B_g \\ -B_g & B_g \end{bmatrix}\begin{Bmatrix} \dot{x}_3 \\ \dot{x}_{3m} \end{Bmatrix} + \begin{bmatrix} C_3 + k_m & -k_m \\ -k_m & k_m \end{bmatrix}\begin{Bmatrix} x_3 \\ x_{3m} \end{Bmatrix} = \begin{Bmatrix} f_{e3} \\ 0 \end{Bmatrix} \tag{2.13}$$

In regular waves, the motions of the floater, the internal mass, as well as the wave excitation force are time-harmonic:

$$x_i = \Re\left\{a_i e^{-i\omega t}\right\} i = 3 \text{ or } 3m \tag{2.14}$$

$$f_{e3} = \Re\left\{A_w X_3 e^{-i\omega t}\right\} \tag{2.15}$$

where a_3 and a_{3m} are complex motion amplitudes of the floater and internal mass, respectively. Inserting Eq. (2.14) and Eq. (2.15) into

[2] For the specific geometry used in Fig. 2.2, Eq. (2.10) gives $\omega_3 \approx 4.22\ rad/s$, (or $\overline{\omega}_3 \equiv \omega_3\sqrt{a/g} \approx 0.61$), $\overline{\mu}_{33}(\overline{\omega}_3) \approx 0.274$. Particulars of this geometry are shown in Appendix A.

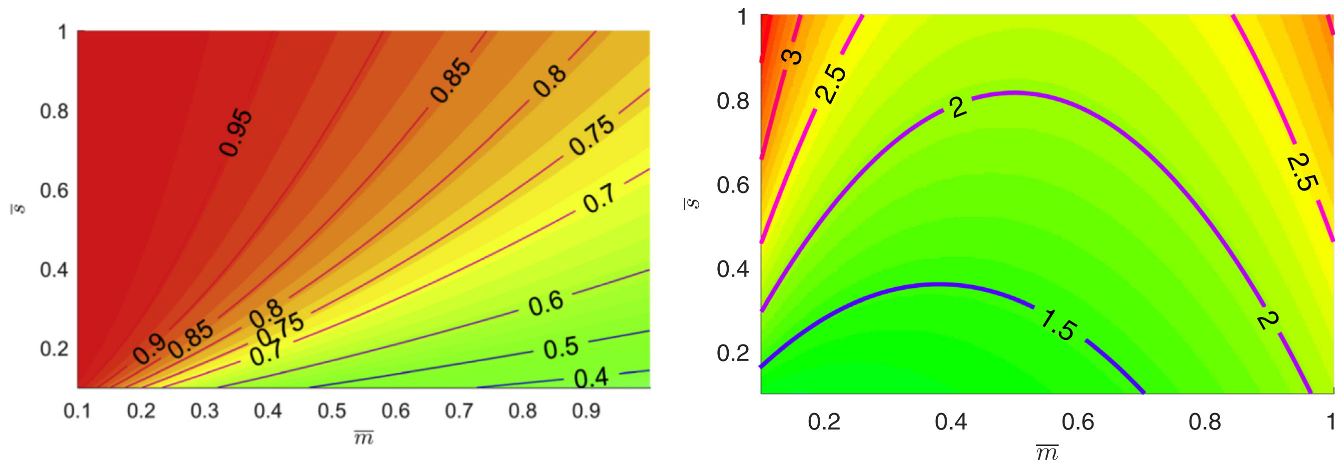

Fig. 2.3. Contours of non-dimensional resonance frequencies: (a) $\overline{\Omega}_1$ and (b) $\overline{\Omega}_2$with varying spring $\bar{s}$ and mass $\overline{m}$.

Eq. (2.13), we obtain the following explicit expressions for the response per unit amplitude of incident wave:

$$\begin{Bmatrix} a_3/A_w \\ a_{3m}/A_w \end{Bmatrix} = \frac{X_3}{\det[Z]}\begin{Bmatrix} -\omega^2 m + k_m + i\omega B_g \\ k_m + i\omega B_g \end{Bmatrix} \tag{2.16}$$

where the matrix [Z] is given by:

$$[Z] = \begin{bmatrix} -\omega^2 M' + (C_3 + k_m) + i\omega(\lambda_T + B_g) & -k_m - i\omega B_g \\ -k_m - i\omega B_g & -\omega^2 m + k_m + i\omega B_g \end{bmatrix} \tag{2.17}$$

with det [Z] being the complex determinant. The Response Amplitude Operator (RAO) of the relative motion, between the internal mass and floater, and the floater itself are:

$$RAO_r \equiv \left|\frac{a_r}{A_w}\right| = \left|\frac{a_{3m} - a_3}{A_w}\right|, \qquad RAO_3 \equiv \left|\frac{a_3}{A_w}\right| \tag{2.18}$$

The time-averaged power extraction by the PTO damper B_g from the internal mass is driven by the relative motion:

$$P_M(\overline{\omega})) = \frac{1}{T}\int_0^T B_g|\dot{a}_r|^2 dt = \frac{1}{2}M\omega_3^3 A_w^2 \times \overline{B}_g\overline{\lambda}_T(\overline{\omega}_3)\overline{\omega}^2 RAO_r^2 \tag{2.19}$$

where $\overline{\lambda}_T(\overline{\omega}_3) = \lambda_T(\omega_3)/\omega_3\pi\rho a^2 d$ is the total nondimensional damping ratio ($\approx$0.032 for the selected geometry) at the resonance frequency of the floater alone at ω_3 without internal mass, $\overline{B}_g \equiv B_g/\lambda_T(\omega_3)$ is the damping ratio of the generator to fluid damping, $\overline{\omega} = \omega\sqrt{a/g}$ is the non-dimensional wave frequency.

The time-averaged wave power per unit width of wave front is well-known:

$$P_W = \frac{\rho g A_w^2}{2} V_g \tag{2.20}$$

where $V_g = \frac{1}{2}V_p[1 + 2k_0h/\sinh(2k_0h)]$ is the group velocity and $V_p = (g/\omega)\tanh(k_0h)$ is the phase velocity of the wave. From Eqs. (2.19) and (2.20), the energy capture width of the system (normalized by the floater diameter) can be defined as:

$$\overline{C}_w = \frac{P_M}{2P_W a} \tag{2.21}$$

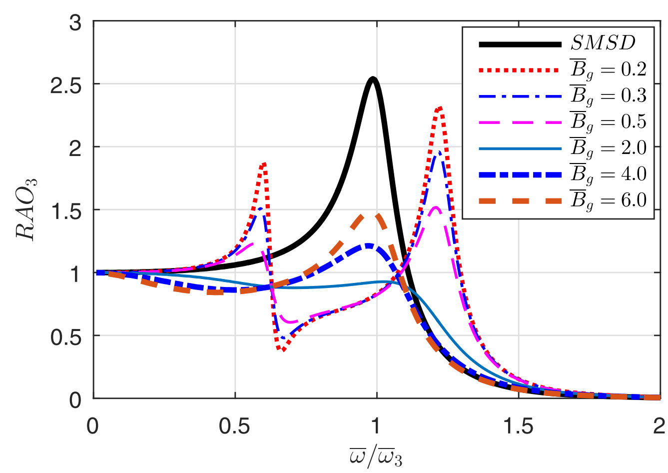

Fig. 2.4. Floater motion RAO with $\overline{m} = 0.3$, $\bar{s} = 0.1$ and varying $\overline{B}_g$.

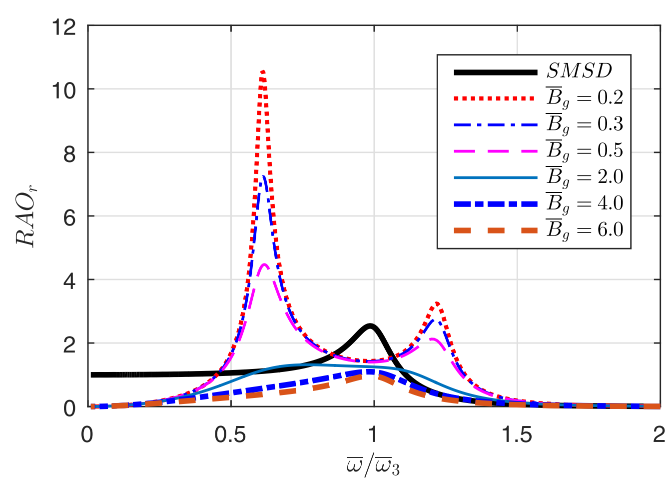

Fig. 2.5. Relative motion RAO with $\overline{m} = 0.3$, $\bar{s} = 0.1$ and varying $\overline{B}_g$.

Hence, the non-dimensional capture width is a function of mass ratio $\overline{m}$, spring ratio $\bar{s}$ and PTO damping ratio $\overline{B}_g$, that is, $\overline{C}_w = \overline{C}_w(\overline{m}, \bar{s}, \overline{B}_g)$. The three parameters determine the interim result of RAO_r before it is used in (2.21).

To study the influence of the mass ratio $\overline{m}$, spring ratio $\bar{s}$ and

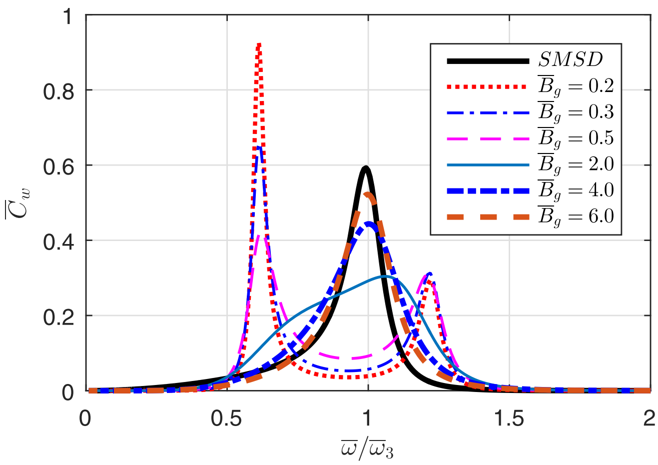

Fig. 2.6. Non-dimensional Capture width $\overline{C}_w$ with $\overline{m} = 0.3$, $\overline{s} = 0.1$ and varying $\overline{B}_g$.

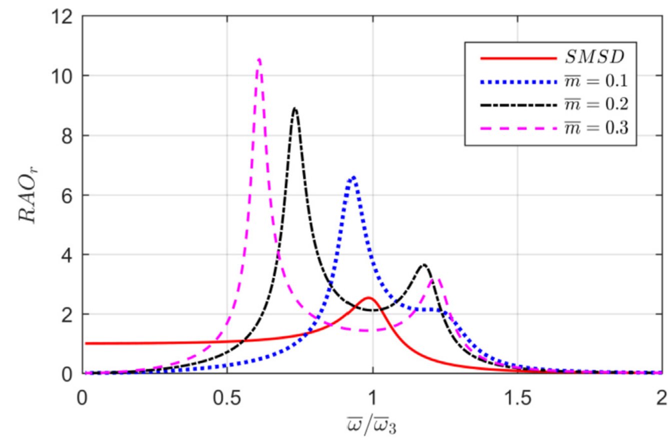

Fig. 2.8. Relative motion RAO with $\overline{s} = 0.1$, $\overline{B}_g = 0.2$ and varying $\overline{m}$.

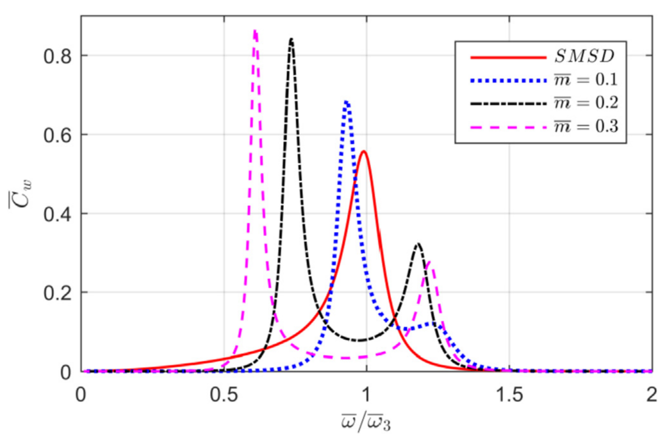

Fig. 2.9. Non-dimensional capture width $\overline{C}_w$ with $\overline{s} = 0.1$, $\overline{B}_g = 0.2$ and varying $\overline{m}$.

generator damping ratio $\overline{B}_g$ on the motion and power response of the Dual-MSD WEC, it is appropriate to recall the traditional heave point absorber concept (Single-MSD or SMSD [4].) for comparison. PTO system is hidden inside the floater for Dual-MSD concept but the Single-MSD concept needs a reference point for motion (which may be the seabed or on-shore structure etc.). For the SMSD, it is a well-known conclusion that the power is maximized when $B_g = \lambda_T$ at resonance (see e.g. Ref. [18]). We take the radius and the draft of the SMSD as a and d respectively, which are same as the Dual-MSD, so that the resonance frequency of the floater is the same. In each of these studies, we present the RAO_3, RAO_r, and C_w computed from Eqs. (2.18) and (2.21).

2.4.1. Effect of PTO damping ratio $\overline{B}_g$

Figs. 2.4–2.6 show that small $\overline{B}_g$ does not change the location of the resonance peaks, but does affect the amplitude of the motion and power response. However, if $\overline{B}_g$ is too large. The two peaks vanish and the troughs in the response of both floater and internal mass evolve to a new peak at the resonance frequency of the floater $\overline{\omega} = \overline{\omega}_3$. This is rather remarkable! In long waves, when wave frequency approaches to $\overline{\omega} \to 0$, RAO_3, the response of the floater of the Dual-MSD, approaches the limit of 1, the same as the traditional Single-MSD WEC. However, for the relative motion, $RAO_r \to 0$ in both high frequency and zero frequency limits. For small enough $\overline{B}_g$, a larger capture width is attainable at longer wave period.

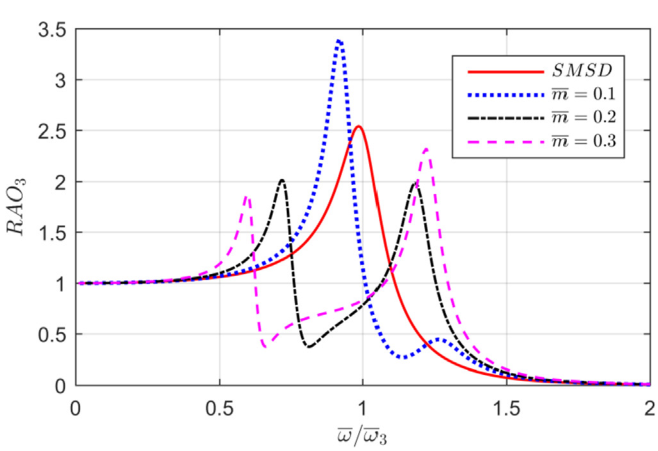

Fig. 2.7. Floater motion RAO with $\overline{s} = 0.1$, $\overline{B}_g = 0.2$ with varying $\overline{m}$.

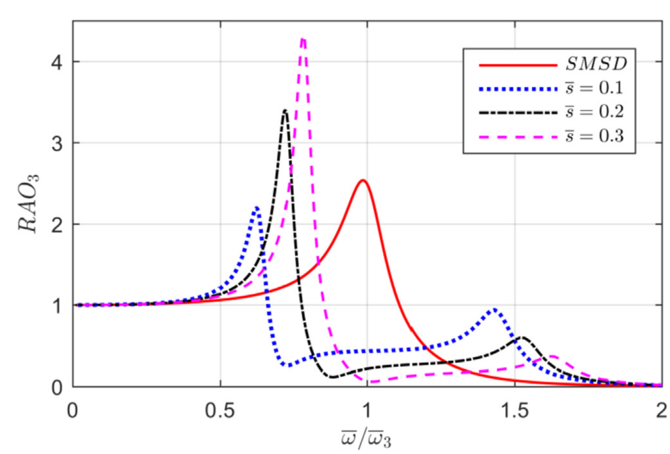

Fig. 2.10. Floater motion RAO with $\overline{m} = 0.5$, $\overline{B}_g = 0.5$ and varying $\overline{s}$.

2.4.2. Effects of mass ratio $\overline{m}$ and internal spring constant $\overline{s}$

Figs. 2.7–2.9 show that $\overline{m}$ not only can change the location of the resonance frequency but also the amplitude of RAOs, thus the capture width. The lower resonance frequency $\overline{\Omega}_1$ is more sensitive to the value of $\overline{m}$.

Figs. 2.10–2.12 show similar behavior as that due to the mass ratio $\overline{m}$, namely, spring ratio $\overline{s}$ can change both the location of the

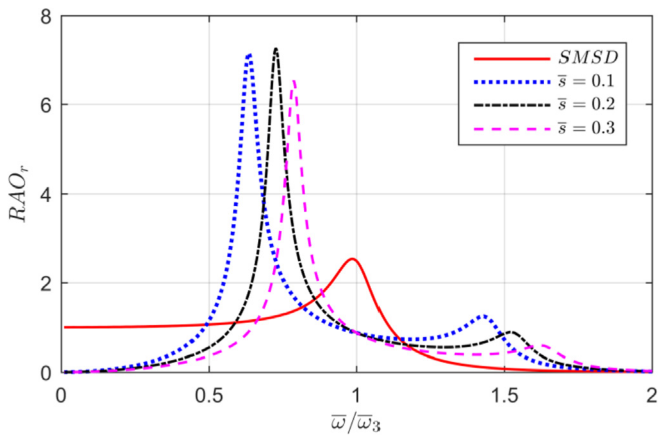

Fig. 2.11. Relative motion RAO with $\overline{m}=0.5$, $\overline{B}_g=0.5$ and varying $\bar{s}$.

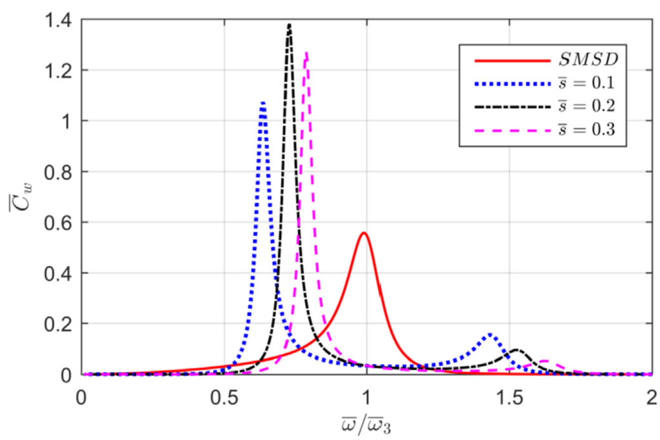

Fig. 2.12. Non-dimensional capture width $\overline{C}_w$ with $\overline{m}=0.5$, $\overline{B}_g=0.5$ and varying $\bar{s}$.

resonance frequency and the amplitude of the motion and power response. However, the effect of $\bar{s}$ is highly non-linear as opposed to $\overline{m}$. Experimental validation in the shift in resonance peaks are shown in Appendix B, which lends credence to this theoretical model.

2.5. Optimizing capture width of the Dual-MSD

2.5.1. Damping ratio optimization

To optimize the capture width $\overline{C}_w$ for a given wave frequency ϖ, we first consider determining the optimal damping ratio $\overline{B}_g$. Equation (2.21) can be rearranged into the following quotient form:

$$\overline{C}_w=\frac{E}{2P_W a}\frac{\overline{B}_g}{\left(A+B\overline{B}_g\right)^2+\left(C+D\overline{B}_g\right)^2} \tag{2.22}$$

where

$$A=\varpi^2(1+\overline{\mu}_{33}(\varpi)-\overline{m})\overline{m}+\frac{(1+\overline{\mu}_{33})^2\bar{s}}{\varpi^2}-[\bar{s}(1+\overline{\mu}_{33}(\varpi))+\overline{m}](1+\overline{\mu}_{33}) \tag{2.23}$$

$$B=-\varpi\overline{\lambda}_T(\varpi)\overline{\lambda}_T \tag{2.24}$$

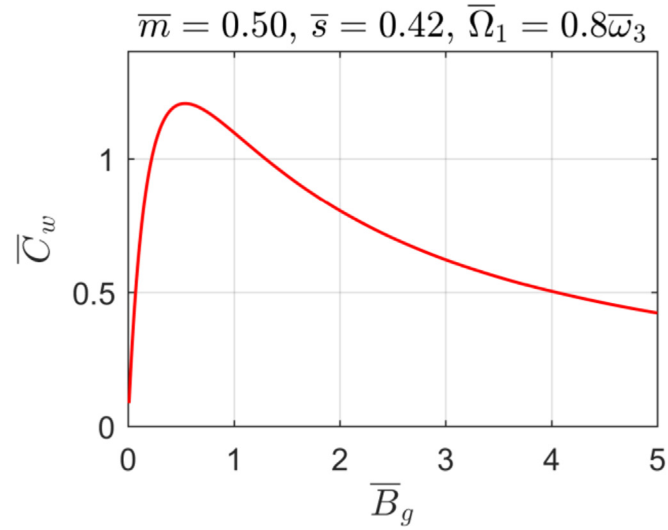

Fig. 2.13. Capture-width ratio versus the PTO damping ratio, taking $\overline{m}=0.50$, $\bar{s}=0.42$ and resonance frequency $\overline{\Omega}_1=0.8\overline{\omega}_3$ as an example.

$$C=\overline{\lambda}_T(\varpi)\left[(1+\overline{\mu}_{33})\bar{s}-\varpi^2\overline{m}\right] \tag{2.25}$$

$$D=(1+\overline{\mu}_{33})\frac{1}{\varpi}\overline{\lambda}_T-\varpi\overline{\lambda}_T(\varpi)(1+\overline{\mu}_{33}(\varpi)) \tag{2.26}$$

$$E=\frac{1}{2}M\omega_3^3|A_W|^2\overline{\lambda}_T\varpi^2|X_3|^2[(1+\overline{\mu}_{33})\overline{m}]^2 \tag{2.27}$$

where $\overline{\lambda}_T$ and $\overline{\mu}_{33}$ without the frequency argument are understood to be the total damping coefficient and the added-mass coefficient, respectively, at the resonance frequency of *the stand-alone floater* $\overline{\omega}_3$.

As illustrated in Fig. 2.13 typically, as $\overline{B}_g$ varies, $\overline{C}_w$ first increase then decrease, and only one maximum exists.

We can differentiate Eq. (2.22) with respect to $\overline{B}_g$ and set it to zero to obtain the optimal $\overline{B}_{g\_opt}$:

$$\frac{\partial\overline{C}_w}{\partial\overline{B}_g}=\frac{E}{2P_W a}\frac{(A^2+C^2)-(B^2+D^2)\overline{B}_g^2}{\left[\left(A+B\overline{B}_g\right)^2+\left(C+D\overline{B}_g\right)^2\right]^2}=0 \tag{2.28}$$

$$\overline{B}_{g\_opt}=\sqrt{\frac{A^2+C^2}{B^2+D^2}} \tag{2.29}$$

Furthermore, if we substitute Eq. (2.29) into Eq. (2.22), we can obtain the *optimal capture width* as:

$$C_{w\_opt}=\frac{E}{4P_W a}\frac{1}{\sqrt{(A^2+C^2)(B^2+D^2)}+(AB+CD)} \tag{2.30}$$

Subsequent to derivation of these exact optimal expressions, they were also applied to a double-float WEC problem in Zhang et al. [22].

2.5.2. Optimization procedure for capture width without limitations on motion

To conduct the optimization of capture with for a given wave frequency ϖ (say, $\varpi=0.8\overline{\omega}_3$, for example), first, we tune the mass ratio and the spring ratio to achieve the resonance frequency of the

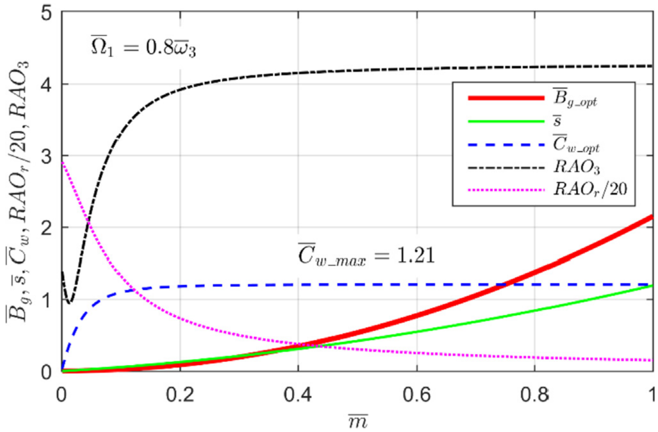

Fig. 2.14. Optimized $\overline{C}_w$ curve and corresponding $\overline{B}_g$, $\overline{s}$, RAO_r and RAO_3 curves with lower resonance frequency $\overline{\Omega}_1 = 0.8\overline{\omega}_3$.

DMSD system to match the wave frequency $\overline{\Omega}_1 = \overline{\omega} = 0.8\overline{\omega}_3$ using Eq. (2.12). In section 2.3, it was already pointed out that the capture width is a function of mass ratio, spring ratio, generator-damping ratio, i.e, $\overline{C}_w = \overline{C}_w(\overline{m}, \overline{s}, \overline{B}_g)$ for a given wave frequency. Next, putting the optimized damping ratio of Eq. (2.29) into Eq. (2.21), we can obtain the optimal capture width as a function of the mass ratio and spring ratio, namely, $\overline{C}_{w\_opt} = \overline{C}_{w\_opt}(\overline{m}, \overline{s})$. However, for a given frequency, the spring ratio is a function of the mass ratio $\overline{s} = Q(\overline{m})$ (as mentioned in section 2.3). Hence, the optimal capture width becomes a function of only the mass ratio $\overline{C}_{w\_opt} = \overline{C}_{w\_opt}(\overline{m}, Q(\overline{m}))$. Thus, we can display the optimal capture width versus mass ratio and with the matching optimal damping ratio, spring ratio, floater RAO, and relative motion RAO all in one figure. Fig. 2.14 illustrates that as $\overline{m}$ increases, the optimized $\overline{B}_g$ and $\overline{s}$ increase, the RAO_r decrease, and the $\overline{C}_w$ first increases and then approaches asymptotically $\overline{C}_w = 1.21$, for the specific sample geometry under consideration. Of interest, we note the plateau behavior of the curve of $\overline{C}_w$ suggests a fairly flexible choice of mass ratio to achieve this value. Different choice of $\overline{m}$, however, leads to different motion responses (both relative motion and floater motion). The most interesting curve is RAO_3. Generally, the RAO_3 curve increases as $\overline{m}$ increases, but when $\overline{m} \to 0$, $RAO_3 \to 1.45$ which corresponds to the case that the Dual-MSD has degenerated to a Single-MSD when $\overline{m}$ is very small. RAO_r is rather large as $\overline{m}$ becomes small, so the discussion following will focus on the $\overline{C}_w$ and RAO_r.

2.5.3. Limitations on design choices of internal mechanical system

When optimizing the capture width of the Dual-MSD, we have to consider several limitations because of the geometry and internal mechanism: these being the relative motion, internal mass, spring, damping, etc. This paper will focus the discussions on two limitations (relative motion and internal mass) because the specific design for changing $\overline{m}$, $\overline{s}$ and $\overline{B}_g$ are separately reported [19].

Here, for illustration, let's consider $\overline{\Omega}_1 = \overline{\omega} = 0.8\overline{\omega}_3$. First, because the internal mass is moving inside the floater of limited space, so the relative motion is limited. Since $\overline{C}_{w\_opt} = \overline{C}_{w\_opt}(\overline{m}, Q(\overline{m}))$, we should select $\overline{m}$ large enough so that the relative motion is less than x_{rmax} while retaining the maximum capture width value $\overline{C}_w = 1.21$, based on Fig. 2.14. If $\overline{x}_{rmax} = x_{rmax}/d = 1.0$, as a cap, it leads to a limitation of relative motion $RAO_{rmax} = \overline{x}_{rmax}/\overline{A}_w = 1/\overline{A}_w$ (Fig. 2.15), where the wave amplitude is non-dimensionalized as $\overline{A}_w = A_w/d$. Furthermore, Fig. 2.14 shows that we can choose a larger $\overline{m}$ for a given wave frequency so that the RAO_r is smaller while the maximum value of $\overline{C}_w$ is still attainable. Thus, for each wave amplitude $\overline{A}_w$, we can interpolate from Fig. 2.14 by using the maximum relative motion criterion: $RAO_{rmax} = 1/\overline{A}_w$ to obtain the corresponding $\overline{B}_g$, $\overline{m}$, $\overline{s}$, and $\overline{C}_w$ (Fig. 2.15). Thus, Fig. 2.15 shows that as $\overline{A}_w$ increases, the RAO_{rmax} decreases, and accordingly, the optimal $\overline{B}_g$, $\overline{m}$ and $\overline{s}$ increase while $\overline{C}_w$ can retain the maximum value. This suggests a larger internal mass ratio $\overline{m}$ is more favorable. In other words, the internal mass does not need to be varied in real application, and it should be the larger the better.

Second, Fig. 2.15 illustrates that the mass ratio $\overline{m}$ could be too large to be practical for higher wave amplitude $\overline{A}_w$. For example, if $\overline{A}_w = 0.25$ then the limitation of relative motion $RAO_{rmax} = 4.0$, which will give the optimized mass ratio (from Fig. 2.15) as $\overline{m} = 0.76$ under this relative motion criterion. The remedy then is to introduce a maximum of mass ratio $\overline{m}_{max}$. If $\overline{m}_{max} = 0.5$, is taken as the choice, then, at same wave amplitude $\overline{A}_w = 0.25$, we simply have to increase the damping ratio rather than having an impractically large mass ratio ($\overline{m} = 0.76$) to meeting the relative motion $RAO_{rmax} = 4.0$. In this situation, the PTO damping would not be the optimal damping (from Eq. (2.29)) anymore, so the capture width cannot achieve the maximum value $\overline{C}_w = 1.21$. Fig. 2.16 shows the final achievable value of $\overline{C}_w$ and corresponding RAO_{rmax}, $\overline{B}_g$, $\overline{m}$, and $\overline{s}$ under concurrently the relative motion limitation and maximum

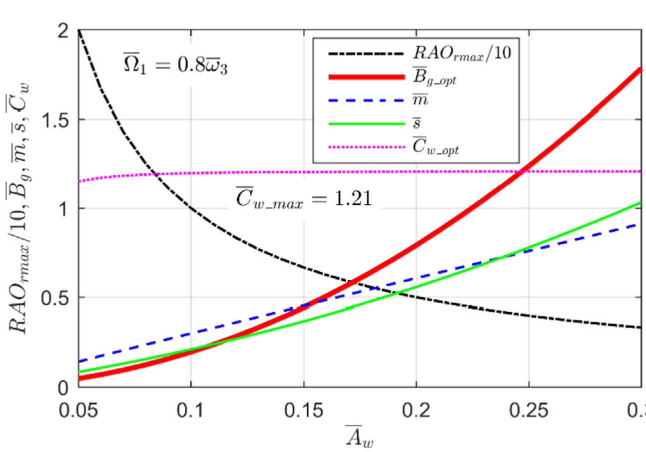

Fig. 2.15. Maximum relative motion RAO_{rmax} and the corresponding $\overline{B}_g$, $\overline{m}$, $\overline{s}$, and $\overline{C}_w$, as a function of wave amplitude $\overline{A}_w$ when $\overline{\Omega}_1 = 0.8\overline{\omega}_3$.

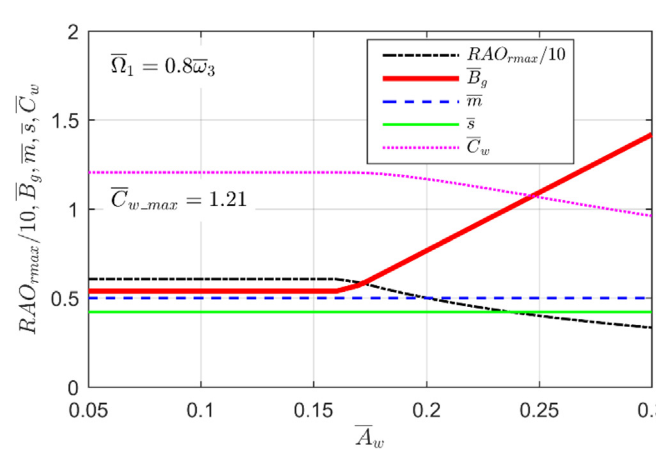

Fig. 2.16. Optimal $\overline{B}_g$, $\overline{m}$, and $\overline{s}$, and corresponding $\overline{C}_w$, RAO_{rmax} as a function of wave amplitude $\overline{A}_w$ when $\overline{\Omega}_1 = 0.8\overline{\omega}_3$ and $\overline{m}_{max} = 0.5$.

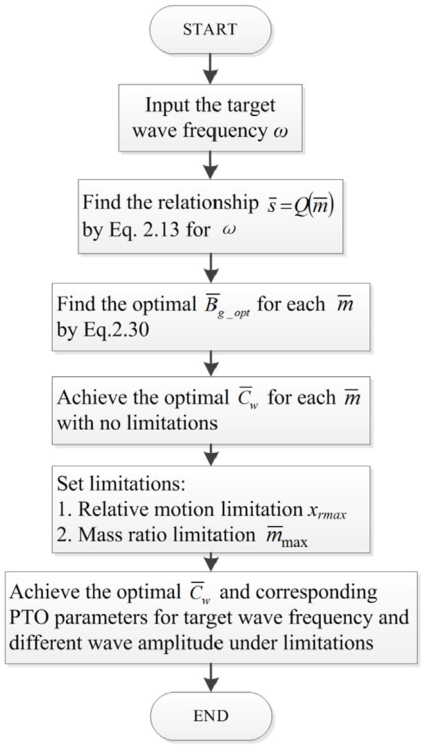

Fig. 2.17. Flow chart of finding the optimal $\overline{C}_w$ and corresponding PTO parameters for a target wave frequency and different wave amplitude under limitations.

mass ratio limitation. Note that the capture width remains optimal at smaller wave amplitude but decreases at largre wave amplitude because of the mass-ratio limitation. Since wave power is proportional to $\overline{A}_w^2$ a small drop in $\overline{C}_w$ still retains significant amount of energy capture.

2.5.4. Optimization for different incident wave frequency and wave amplitude under motion limitations

The above optimization procedure is summarized in Fig. 2.17 as a flow chart. Following the same procedure, we can plot the optimal $\overline{C}_w$ in terms of wave amplitude $\overline{A}_w$ and target wave frequency $\overline{\omega}$ in Fig. 2.18 under both relative motion limitation and mass ratio limitation. Each dot in Fig. 2.18 is the optimized capture width ratio (under limitations) at given wave frequency and amplitude, with the $\overline{m} = \overline{m}_{\max}$ but the $\overline{s}$ and the $\overline{B}_g$ varying. It seems that we do not have to change the mass ratio but only varying the spring ratio to match the resonance frequency of the DMSD to the encounter wave frequency. Nevertheless, the limitations considered in this paper are just relative motion and mass ratio, there may be other limitations in spring or damping systems too [19,20]. Thus, in practice, all of these three parameters ($\overline{B}_g$, $\overline{m}$, $\overline{s}$) may have to be changeable. Also, from Fig. 2.18, the optimal $\overline{C}_w$ is not only a function of wave frequency, but also wave amplitude. Additionally, comparing to SMSD, Dual-MSD's have larger capture width especially in lower wave frequencies.

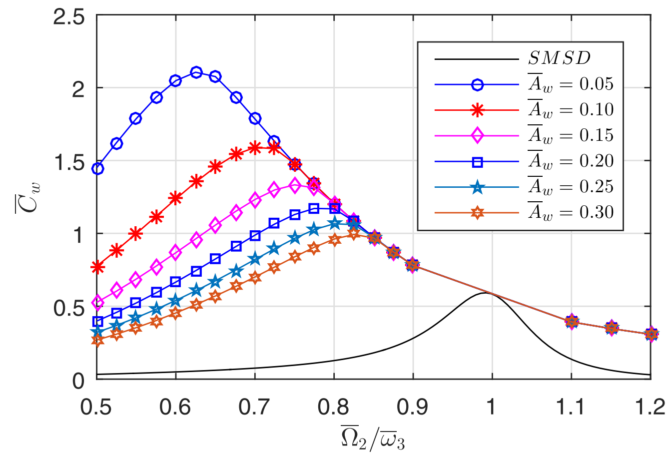

Fig. 2.18. Optimal $\overline{C}_w$ curves for different target wave frequency $\overline{\omega}$ and varying wave amplitude $\overline{A}_w$.

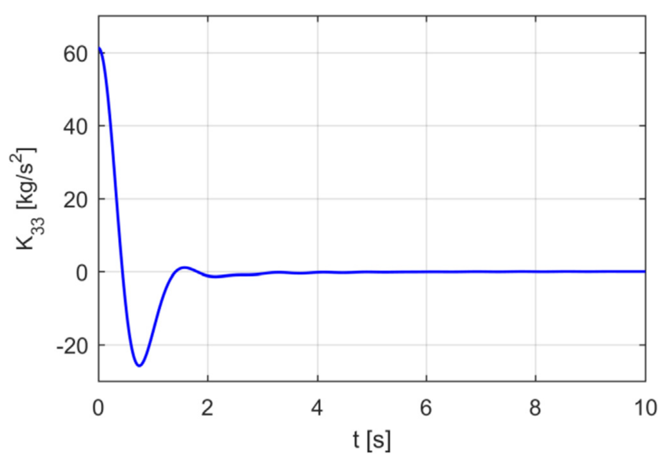

Fig. 3.1. Retardant function of the floater in heave mode.

3. Time-domain analysis in irregular waves

The motion and power response on the average in irregular waves are different from the regular-wave cases addressed earlier. Since waves in the open sea are random or irregular, it is of practical interest to understand how to model this system in irregular waves. Further, in order to confine the excessive relative motion in irregular wave, an end-stop device should be employed, which time domain simulation is needed.

3.1. Equation of motion in the time domain

The impulse response function method (IRF) [12] can be used to calculate the motion and power response in the time domain. Eq. (3.1) is the coupled equation of motion for Dual-MSD in the time domain.

$$\begin{cases} (M_{33} - m + \mu_{33\infty})\ddot{x}_3 + \int_0^t K_{33}(t-\tau)\dot{x}_3(\tau)d\tau + B_g\dot{x}_3 + (C_3 + k_m) - B_g\dot{x}_{3m} - k_m x_{3m} = f_{e3}(t) \\ m\ddot{x}_{3m} + B_g\dot{x}_{3m} + k_m x_{3m} - B_g\dot{x}_3 - k_m x_3 = 0 \end{cases} \tag{3.1}$$

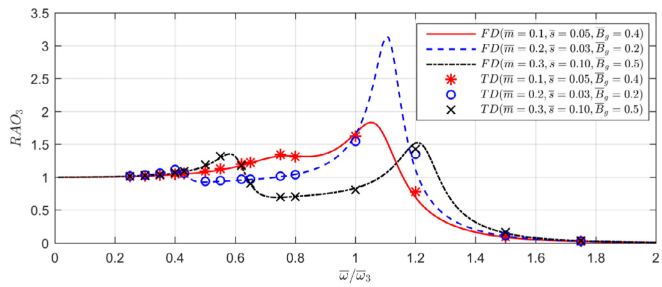

Fig. 3.2. Comparison of floater motion RAO between time domain (TD) and frequency domain (FD).

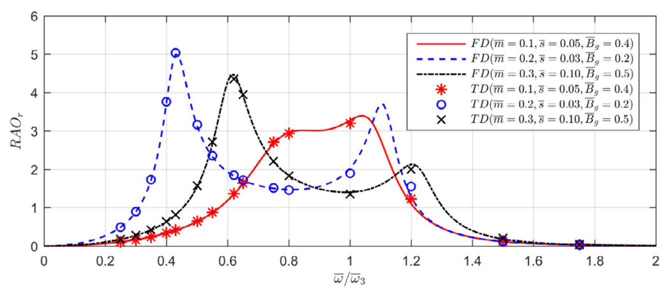

Fig. 3.3. Comparison of relative motion RAO between time domain (TD) and frequency domain (FD).

where $K_{33}(t)$ is the retardant kernel function, which can be calculated from damping by below:

$$K_{33}(t) = \frac{2}{\pi}\int_0^{\infty}[\lambda_T(\omega) - \lambda_T(\infty)]\cos\omega t d\omega \tag{3.2}$$

An assumption is made that the viscous correction effects are not frequency-dependent, thus not affecting the normal frequency-domain to time-domain relations. As mentioned before, for the convenience of experiment, the geometry of the floater is $2a/h = 0.271$ and $d/h = 0.288$ (Appendix A). Since time domain calculation is more time-consuming than frequency-domain analysis, so only peak wave frequency $\overline{\omega}_p = 0.8\overline{\omega}_3$ ($\omega_p = 3.38\ rad/s, T_p = 1.86s$) will be explored as an example. The system is treated as a passive device with PTO damping B_g taken as parameter, but constant in value.

To verify the correctness of the time-domain code, the authors compare the time-domain results with those from regular-wave excitation. Fig. 3.1, Fig. 3.2 and Fig. 3.3 are the results of floater motion RAO and relative motion RAO in time domain (dots) and frequency domain (lines). They match well, especially at low wave frequencies, lending confidence to the procedure.

3.2. General irregular wave simulation of a DMSD absorber

Irregular waves response simulations use ISSC spectrum, namely a modified Pierson-Moskowitz spectrum [13], to construct the irregular wave elevation time history $\zeta(t)$.

$$S(\omega) = H_s^2 T_1 \frac{0.11}{2\pi}\left(\frac{\omega T_1}{2\pi}\right)^{-5}\exp\left[-0.44\left(\frac{\omega T_1}{2\pi}\right)^{-4}\right] \tag{3.3}$$

$$T_1 = 0.7713T_p \tag{3.4}$$

$$A(\omega_j) = \sqrt{2S(\omega_j)\Delta\omega} \tag{3.5}$$

$$\zeta(t) = \sum_{j=1}^{N} A(\omega_j)\sin(\omega_j t + \varepsilon_j) \tag{3.6}$$

$$f_{e3}(t) = \sum_{j=1}^{N} |X_3(\omega_j)|A(\omega_j)\sin(\omega_j t + \varphi_j + \varepsilon_j) \tag{3.7}$$

$$P_w = \sum_{j=1}^{N}\frac{\rho g^2}{4\omega_j}A(\omega_j)^2\left[1 + \frac{2k_0(\omega_j)h}{\sinh(2k_0(\omega_j)h)}\right]\tanh(k_0(\omega_j)h) \tag{3.8}$$

where $H_s = 2A_s$ is the significant wave height, $T_p = 2\pi/\omega_p$ is the peak period, $A(\omega_j)$ is the wave amplitude of each frequency component, and ε_j is the random phase angle, which uniformly distributes between $[0, 2\pi]$ and is constant in time. Eq. (3.7) and Eq. (3.8) are the wave excitation force in heave mode and the wave power of irregular wave in unit frontal width.

3.3. Motion response and power capture in irregular waves

In the frequency domain, the optimization procedure was shown in Section 2.5, an example was given in Fig. 2.16 when peak wave frequency is $\overline{\omega}_p = 0.8\overline{\omega}_3$. In the time domain using the same mass ratio $\overline{m}$, spring ratio $\overline{s}$, and damping ratio $\overline{B}_g$ as in Fig. 2.16, Fig. 3.4 and Fig. 3.5 plot the non-dimensional capture width $\overline{C}_w$ and maximum relative motion $\overline{x}_{rmax} = x_{rmax}/d$. Capture width is smaller in irregular waves (maximum $\overline{C}_w$ is around 0.24) than in regular waves (Fig. 2.16). Furthermore, the optimal constant $\overline{B}_g$ in irregular wave is larger than in regular waves. In this $\overline{\omega}_p = 0.8\overline{\omega}_3$ example, the optimal $\overline{B}_g \approx 3.0$. However, the $\overline{C}_w$ is still smaller than that in regular waves. This is because the bandwidth of the capture width of the DMSD WEC is relatively narrow, and irregular waves contain all frequency components. To compensate the reduction because of the narrow bandwidth, a larger PTO damping is in need.

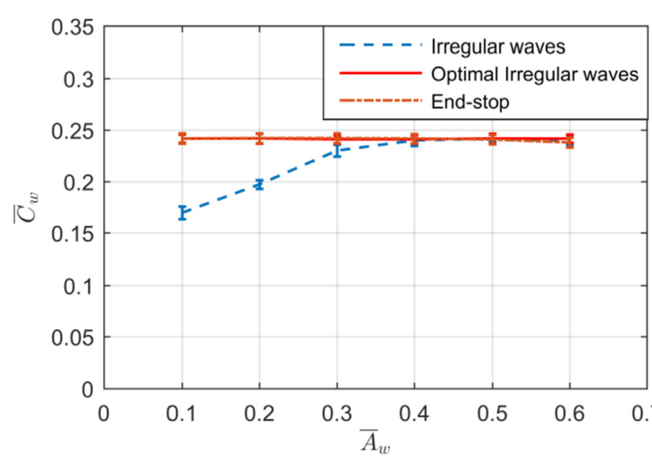

Fig. 3.4. Comparison of non-dimensional capture width $\overline{C}_w$, between time domain results and same mass ratio $\overline{m}$, spring ratio $\overline{s}$ and damping ratio $\overline{B}_g$ for each wave amplitude $\overline{A}_w$, and optimal time domain results with $\overline{B}_g = 3.0$, and with end-stop $\overline{B}_e = 5.0$, $\overline{k}_e = 0.5$, $\overline{L}_e = 0.2$ when peak wave frequency $\overline{\omega}_p = 0.8\overline{\omega}_3$.

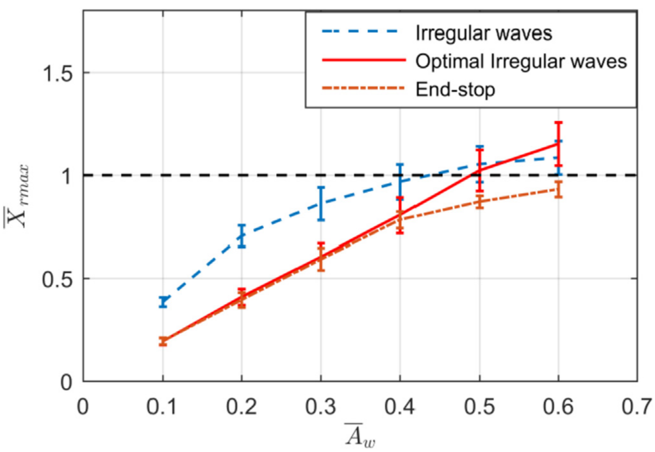

Fig. 3.5. Maximum relative motion $\bar{x}_{rmax}$ and same mass ratio $\bar{m}$, spring ratio $\bar{s}$ and damping ratio $\bar{B}_g$ and using optimal $\bar{B}_g = 3.0$ in irregular wave for each wave amplitude $\bar{A}_w$, and with end-stop $\bar{B}_e = 5.0$, $\bar{k}_e = 0.5$, $\bar{L}_e = 0.2$ when peak wave frequency $\bar{\omega}_p = 0.8\bar{\omega}_3$.

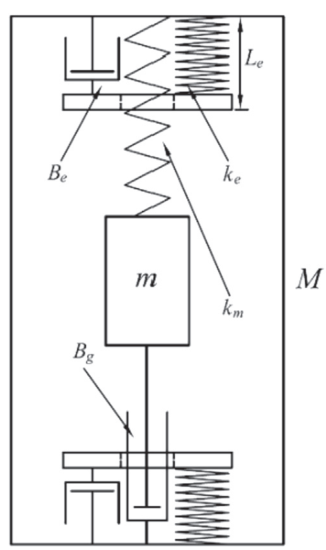

Fig. 3.6. Schematic of the Dual-MSD with end-stop system.

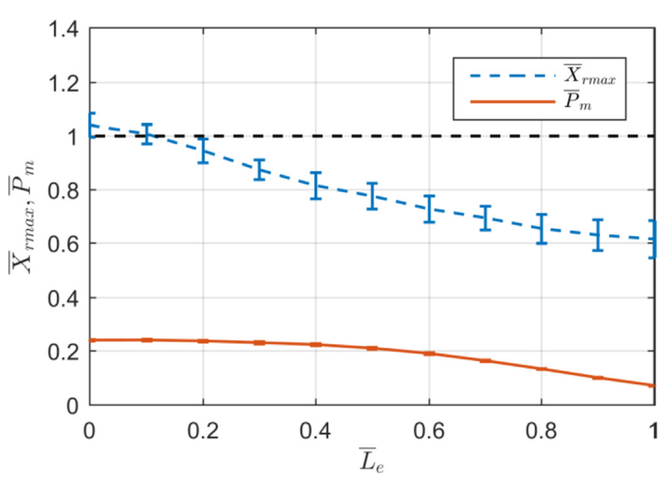

Fig. 3.7. The influence of end-stop length $\bar{L}_e$ on the maximum relative motion $\bar{x}_{rmax}$ and mean power $\bar{P}_m$ response in irregular wave with $\bar{k}_e = 0.1$, $\bar{B}_e = 3.0$, $\bar{m} = 0.5$, $\bar{s} = 0.42$, $\bar{B}_g = 3.0$ and $\bar{A}_s = 0.6$.

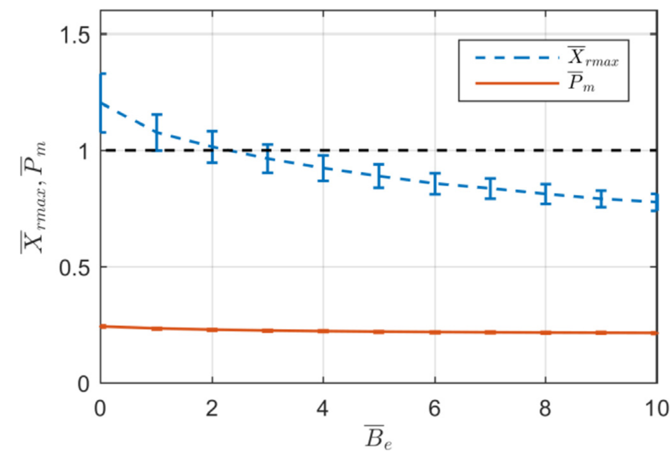

Fig. 3.8. The influence of end-stop damping $\bar{B}_e$ on the maximum relative motion $\bar{x}_{rmax}$ and mean power $\bar{P}_m$ response in irregular wave with $\bar{L}_e = 0.5$, $\bar{k}_e = 0.0$, $\bar{m} = 0.5$, $\bar{s} = 0.42$, $\bar{B}_g = 3.0$ and $\bar{A}_s = 0.6$.

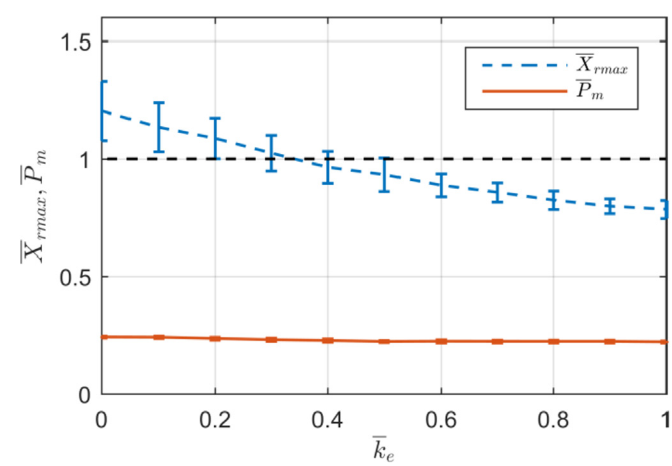

Fig. 3.9. The influence of end-stop spring $\bar{k}_e$ on the maximum relative motion $\bar{x}_{rmax}$ and mean power $\bar{P}_m$ response in irregular wave with $\bar{L}_e = 0.5$, $\bar{B}_e = 0.0$, $\bar{m} = 0.5$, $\bar{s} = 0.42$, $\bar{B}_g = 3.0$ and $\bar{A}_s = 0.6$.

However, even with enlarged optimal PTO damping, the capture width is still lower than that in the regular waves.

Fig. 3.5 illustrates that owing to the irregularity of the waves, the maximum relative motion $\bar{x}_{rmax}$ can be larger than unity even with enlarged optimal $\bar{B}_g$ for irregular waves when the significant wave height is large. Hence an end-stop device is needed to confine the excessive relative motion.

3.4. End-stop modeling and effect

Because the Dual-MSD has an internal mass moving inside the floater, so the relative motion between the internal mass and floater has limitation $\bar{x}_{rmax}$. As mentioned earlier in this work, the maximum relative motion is set at $\bar{x}_{rmax} = x_{rmax}/d = 1.0$. In irregular waves, the relative motion response sometimes exceeds this bond $\bar{x}_{rmax}$ (Fig. 3.5). To limit the relative motion and protect the internal structure, an end-stop must be implied. As shown in Fig. 3.6, the end-stop in this paper is a system consisting of spring and damper, which can be easily achieved by a physical spiral spring and a damper. such as shock absorbers for automobiles. Thus, the end-stop has three parameters: spring constant k_e, damping constant B_e and end-stop length L_e. The normalization of

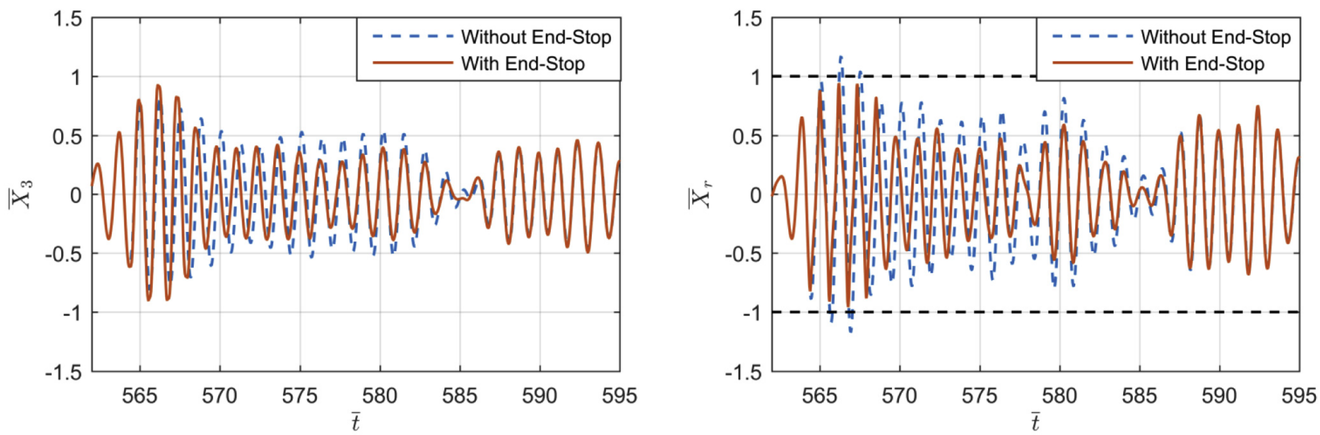

(a) **(b)**

Fig. 3.10. Example of end-stop effect on the floater motion (a) and the relative motion (b), with $\overline{B}_e = 5.0$, $\overline{k}_e = 0.5\overline{L}_e = 0.2$, $\overline{m} = 0.5$, $\overline{s} = 0.42$, $\overline{B}_g = 3.0$ and $\overline{A}_s = 0.6$.

these three parameters are as follows: $\overline{k}_e = k_e/C_3$, $\overline{B}_e = B_e/\lambda_T(\omega_3)$, and $\overline{L}_e = L_e/d$.

In irregular waves, when excessive relative motion occurs, the internal mass hits the end-stop and the end-stop pushes the internal mass by spring and damper to decrease the motion. The effect of length, damping and spring of end-stop are discussed in Fig. 3.10, Fig. B.1, and Fig. B.2, where the mean power is normalized by the wave power in the range of floater width $\overline{P}_m = P_m/2aP_w$. Fig. 3.7 illustrates that as the end-stop length $\overline{L}_e$ increasing, the maximum relative motion $\overline{x}_{r\max}$ decrease as well as the mean power $\overline{P}_m$. The same property is found for end-stop damping $\overline{B}_e$ (Fig. 3.8) and spring $\overline{k}_e$ (Fig. 3.9), but the decreasing rate is very small. The capture width curve is almost flat when the $\overline{B}_e$ and $\overline{k}_e$ is varying in Figs. 3.8 and 3.9. The existence of damping $\overline{B}_e$ consumes energy. The spring $\overline{k}_e$ does not consume energy but changes response property, because the spring constant in the range of end-stop is not optimal anymore. Thus, the most influential parameter is the end-stop length $\overline{L}_e$. The small $\overline{L}_e$ means low possibility of end-stop interfering the movement of the internal mass. Fortunately, with a proper designed end-stop ($\overline{B}_e = 5.0$, $\overline{k}_e = 0.5$, $\overline{L}_e = 0.2$), the relative motion is confined effectively (Fig. 3.5) while the energy absorption does not drop much (Fig. 3.4). In Fig. 3.4, the power response remains almost the same, only have 1–2% declination at $\overline{A}_s = 0.6$. Fig. 3.10 gives an example of time history of the floater motion and the relative motion with and without the end-stops. Clearly, we can see that when the wave force is small, the relative motion does not reach the end-stop, so that the motion response is the same with and without end-stop. Nevertheless, when the wave force is larger, the relative motion becomes larger and the internal mass hit the end-stop. Because of the spring and damping of the end-stop the internal mass is pushed back so that the relative motion is limited. At the same time, the motion of floater becomes larger due to the force of the end-stop. As time progresses, the waves force becomes smaller again and the responses of the motions become the same with and without end-stop. We note that elaborate control of such constrained system in the time domain had been developed using Nonlinear Model-Predictive Control (Son & Yeung [21])

4. Conclusions

Owing to the coupling effects between the two sets of mass-spring-damper in the Dual-MSD WEC, the response of motions and power have two resonance peaks, which can be manipulated by varying the internal mass and spring. Thus, building a relatively small (economical) device but working in lower wave frequencies is possible. The damping does not influence the locations of the resonance much, but to achieve optimal wave energy capture width, the damping of the PTO also needs to be adjustable, based on a new formula that has been developed. When optimizing the capture width, there are limitations (such as relative motion, internal mass, spring and damping etc.) which come from the geometry of the floater and internal mechanisms. In this paper, the limitations being considered are the relative motion and internal mass. Under these two limitations and using regular waves in the frequency domain, the optimal capture width turns out to be not only a function of wave frequency but also wave amplitude. The IRF method is used to simulate the motion and power response in irregular waves in time domain. It turns out that the mean power $\overline{P}_m$ is smaller in irregular waves than that in regular waves, because of the narrow bandwidth of the capture width curve and the use of a constant PTO damping. Excessive relative motion occurs because of the irregular behavior of the waves. To limit the excessive relative motion, an end-stop is employed. With a properly designed end-stop, there is very little energy loss (less than 2%). The frequency-domain results of the model have been validated by a specially designed DMSD WEC fitted with "The Berkeley Wedge" bottom.

Acknowledgments

We are grateful to members of The Berkeley Marine Mechanics Laboratory (BMML) for their invaluable assistance during the course of this research, which constitutes part of the dissertation work of the first author. Financial support for his visit was provided by Harbin Engineering University under the Natural Science Foundation of China, Grant #51409066 &11572094 and the China-UK international collaborative Grant # (NSFC-EPSRC/NERC) 5171101175. Results of validation of this theory as provided in Appendix B are through the courtesy of L. Virey and M. Park, who were supervised by Asst. Professor S. Makiharju and supported by the Moritz Jaehne Memorial Fund and the American Bureau of Shipping of UC Berkeley. Partial support by the American Bureau of Shipping via an endowed chair held by the correspondence author R.W. Yeung is gratefully acknowledged.

Appendix A

Table of particulars of the floater for illustrative computations.

Diameter	$2a$	16	inch
Draft	d	17	inch
Water depth	h	59.1	inch
Resonance frequency	ω_3	4.22	rad/s
Resonance Period	$2\pi/\omega_3$	1.48	s
Added mass coefficient at resonance	$\overline{\mu}_{33}(\omega_3)$	0.2742	–
Radiation damping coefficient at resonance	$\overline{\lambda}_{33}(\omega_3)$	0.0324	–
Viscous correction (flat-bottom)	f_{vis}	1.753	–

Appendix B. Experimental validation of modeling of a variable resonance-frequency WEC device.

Figure B.1 below, courtesy of Virey and Park [19,20] shows a comparison of the responses from the theory as presented and those from a variable frequency-resonance WEC, which was specially fitted with a Berkeley-Wedged shape bottom [14] (see Figure B.2), undergoing a one-degree of freedom motion. The measured value of f_{vis} was 1.543 for this shape. Details of the design to achieve specific values of $\bar{s}, \overline{m}$, and hydraulic-cylinder power takeoff $\overline{B}_g$ (labeled as $\overline{B}_T$) are described in Refs. [19,20].

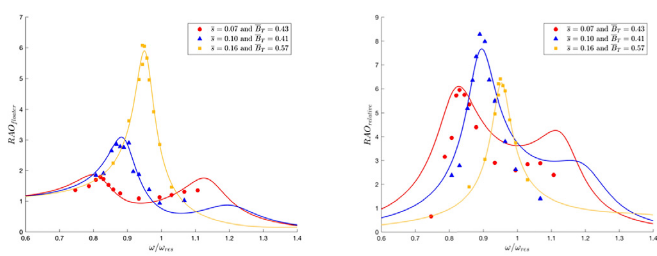

(a) Floater motion (b) Relative motion

Fig. B.1. Measured response for WEC device shown in Fig. B.2, at $\overline{m} = 0.1062$, with varying $\bar{s}$.

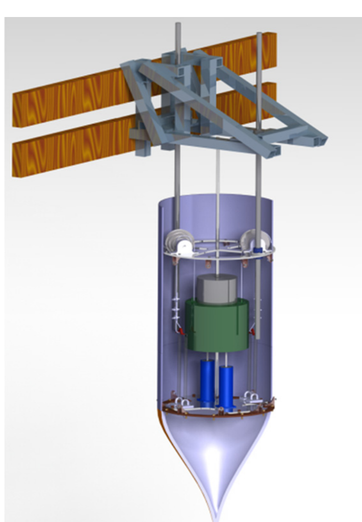

Fig. B.2. Rendering of DMSD-WEC device in wave-excited heaving motion mounted on a platform.

References

[1] G. Mørk, S. Barstow, A. Kabuth, Assessing the global wave energy potential, *Proceedings*, ASME 29th international conference on ocean, offshore and arctic engineering, Am. Soc. Mech. Eng. (2010) 447–454, https://doi.org/10.1115/omae2010-20473.
[2] K. Gunn, C. Stock-Williams, Quantifying the global wave power resource, Renew. Energy 44 (2012) 296–304, https://doi.org/10.1016/j.renene.2012.01.101.
[3] A.O. Falcao, Wave energy utilization: a review of the technologies, Renew. Sustain. Energy Rev. 14 (3) (2010) 899–918, https://doi.org/10.1016/j.rser.2009.11.003.
[4] E.E. Bachynski, Y.L. Young, R.W. Yeung, Analysis and optimization of a tethered wave energy converter in irregular waves, Renew. Energy 48 (2012) 133–145, https://doi.org/10.1016/j.renene.2012.04.044.
[5] N. Tom, R.W. Yeung, Experimental confirmation of nonlinear-model-predictive control applied offline to a permanent magnet linear generator for ocean-wave energy conversion, IEEE J. Ocean. Eng. 41 (2) (2015) 281–295, https://doi.org/10.1109/joe.2015.2439871.
[6] P.C. Parks, Wedges, Plates and Waves Some Simple Mathematical Models of Wave Power Machines, Power from Sea Waves, Academic Press, 1980, pp. 251–285.
[7] M.J. French, R. Bracewell, Heaving Point Absorbers Reacting against an Internal Mass, Hydrodynamics of Ocean Wave-energy Utilization, Springer Berlin Heidelberg, 1986, pp. 247–255, https://doi.org/10.1007/978-3-642-82666-5_21.
[8] R.V. Chaplin, M.J. French, R.H. Bracewell, An Improved Version of PS Frog, Proceedings, Second European Wave Energy Conference, 1995, pp. 345–350. Lisbon, Portugal.
[9] L. Wang, D. Son, R.W. Yeung, On the performance of a dual-cylinder wave-energy converter: single versus two degrees of freedom, in: Proceedings, 35th International Conference on Ocean, Offshore and Arctic Engineering, June 2016, p. 9, https://doi.org/10.1115/omae2016-54422. Paper # OMAE2016–54422.
[10] U.A. Korde, Use of oscillation constraints in providing a reaction for deep water floating wave energy devices, in: Proceedings, the Tenth International Offshore and Polar Engineering Conference, International Society of Offshore and Polar Engineers, 2000.
[11] U.A. Korde, Systems of reactively loaded coupled oscillating bodies in wave energy conversion, Appl. Ocean Res. 25 (2) (2003) 79–91, https://doi.org/10.1016/s0141-1187(03)00044-0.
[12] W.E. Cummins, The Impulse Response Function and Ship Motions, David Taylor Model Basin, Washington DC, 1962. Report #1661.
[13] O.M. Faltinsen, Sea Loads on Ships and Offshore Structures, Cambridge University Press, Cambridge, UK, 1990.
[14] F. Madhi, M.E. Sinclair, R.W. Yeung, The Berkeley Wedge: an asymmetrical energy-capturing floating breakwater of high performance, Marine Systems & Ocean Technology, Journal of SOBENA 9 (1) (2014) 05–16.
[15] R.W. Yeung, Added mass and damping of a vertical cylinder in finite-depth waters, Appl. Ocean Res. 3 (3) (1981) 119–133, https://doi.org/10.1016/0141-1187(81)90101-2.
[16] D. Son, V. Belissen, R.W. Yeung, Performance validation and optimization of a dual coaxial-cylinder ocean-wave energy extractor, Renew. Energy 92 (2016) 192–201, https://doi.org/10.1016/j.renene.2016.01.032.
[17] C. Cochet, Hydrodynamic performance of a compound cylinder extracting ocean-wave energy, Trans. - Soc. Nav. Archit. Mar. Eng. 120 (2013) 395–415.
[18] R.W. Yeung, A. Peiffer, N. Tom, T. Matlak, Design, analysis, and evaluation of the UC-Berkeley wave-energy extractor, ASME J. Offshore Mech. Arct. Eng. Trans 134 (2) (2012) 021902, https://doi.org/10.1115/omae2010-20492.
[19] L. Virey, Design and Evaluation to a Variable Resonance-frequency Wave-energy Converter, M.S. Thesis, Dept. of Mechanical Engineering, University of California at Berkeley, December, 2016.
[20] M. Park, Fabrication and Validation of a Variable Resonance-frequency Wave-energy Converter, M.S. Thesis, Dept. of Mechanical Engineering, University of California at Berkeley, December, 2016.
[21] D. Son, R.W. Yeung, Optimizing ocean-wave energy extraction of a dual coaxial-cylinder WEC using nonlinear model predictive control, Appl. Energy 187 (2017) 746–757, https://doi.org/10.1016/j.apenergy.2016.11.068.
[22] L. Zhang, L.P. Jin, B. Zhou, X. Zheng, H. Liu, Oscillation and conversion performance of a double-float wave energy converter, in: Proceedings of 3rd International Conference for Innovation of Naval Architecture and Marine Engineers, Marine Renewable Energy Sub-Forum (ICNAME 2017-MRE), Sept 7–9, 2017 (Qingdao, China).